ACS APPLIED NANO MATERIALS

www.acsanm.org Article

Halide Effects in $BiVO_4$/BiOX Heterostructures Decorated with Pd Nanoparticles for Photocatalytic Degradation of Rhodamine B as a Model Organic Pollutant

Mary O. Olagunju, Elsayed M. Zahran, Jacqueline M. Reed, Elnaz Zeynaloo, Dharmendra Shukla, Joshua L. Cohn, Bapurao Surnar, Shanta Dhar, Leonidas G. Bachas, and Marc R. Knecht*

Cite This: *ACS Appl. Nano Mater.* 2021, 4, 3262−3272 Read Online

ACCESS | Metrics & More | Article Recommendations | SI Supporting Information

ABSTRACT: In this contribution, a single pot approach was employed to synthesize nanoscale $BiVO_4$/BiOX/Pd, where the halogen was varied over Cl, Br, and I. These materials were used to study the effect of the halide identity in the BiOX nanoplate component for its ability to modulate/maximize the photocatalytic properties of the materials. Once the nanomaterials were fully characterized *via* a suite of approaches, their reactivity for the degradation of rhodamine B, a model pollutant, was examined. All of the materials demonstrated high photocatalytic rates, reaching completion in <10 min in most cases. The results demonstrated that the $BiVO_4$/BiOCl/Pd and $BiVO_4$/BiOBr/Pd have significantly enhanced reactivity compared to the $BiVO_4$/BiOI/Pd structures. Further studies using the $BiVO_4$/BiOBr/Pd in the degradation of rhodamine B in natural water samples indicated that the materials retained their reactivity, demonstrating their potential use in environmental systems.

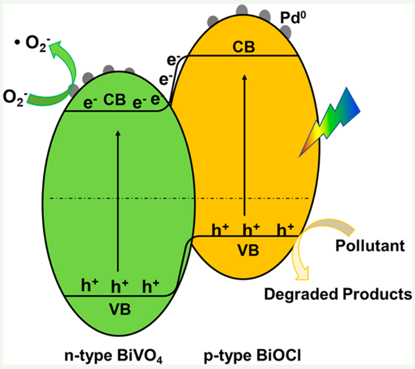

KEYWORDS: *$BiVO_4$, BiOCl, BiOI, BiOBr, halide effects, Pd, photocatalysis*

■ INTRODUCTION

Rapid population growth and industrialization have led to a global energy and environmental situation that requires the development of sustainable approaches to maintain growth in the 21st century.[1] Because of wastewater contamination with organic pollutants, remediation of contaminated water has attracted significant interest.[2] While a variety of approaches have been reported, nanoscale heterogeneous semiconductor photocatalysts have gained attention because of their ability to harness solar energy for the degradation of pollutants.[3] TiO_2 is one of the most studied semiconductor photocatalysts for environmental remediation.[4] Although TiO_2 is efficient, because of its large band gap (3.2 eV), its reactivity is limited to UV light excitation, which accounts for only 4% of the solar spectrum.[4−7] The development of new photocatalysts that exploit a broader range of the solar spectrum is desired and could lead to enhanced environmental remediation for sustainable reactivity.

Recently, bismuth vanadate ($BiVO_4$) has been identified as a promising photocatalyst because of its visible light-driven properties.[8] Of the three main crystal phases of $BiVO_4$, the tetragonal zircon and scheelite phases have a band gap of 3.1 eV, while the monoclinic scheelite has a band gap of 2.4 eV.[9−11] As a result, monoclinic $BiVO_4$ (*m*-$BiVO_4$) has been of great interest because of its narrower band gap, which is anticipated to lead to enhanced photoreactivity.[12,13] Although the band gap is suitable for visible light activation, this n-type photocatalyst has a low separation efficiency of photogenerated electron−hole pairs, thereby limiting its photocatalytic activity.[14,15] Various approaches have been explored to improve the excited charge carriers separation in *m*-$BiVO_4$. For instance, doping $BiVO_4$ catalysts with various species, such as Eu,[16] S,[17] Ag,[18,19] and Fe[20] has shown significant enhancement in their sustainable photocatalytic activity.[2,21] In another strategy, creating heterojunctions between $BiVO_4$ and a second semiconductor has demonstrated improvement in the photocatalytic activity of the heterostructured material.[22,23] This enhanced reactivity arises from tuning of the band gap in the final materials, resulting in diminished charge carrier recombination. For instance, Zhang *et al.* synthesized a $BiVO_4$/TiO_2 heterostructure for the decolorization of rhodamine B (RhB), which showed a higher photocatalytic activity than TiO_2 alone.[24] Yan *et al.* designed a novel $BiVO_4$/Ag_3VO_4 heterojunction for the degradation of RhB, methylene blue (MB), methyl red, and methyl violet. The heterojunction exhibited higher photocatalytic activity than the individual

Received: February 15, 2021
Accepted: February 19, 2021
Published: March 9, 2021

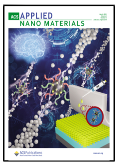

https://dx.doi.org/10.1021/acsanm.1c00481
ACS Appl. Nano Mater. 2021, 4, 3262−3272

Scheme 1. Synthesis Approach for the Production of Nanosized $BiVO_4$/BiOX/Pd Where the Halide Identity can be Varied between Cl, Br, and I

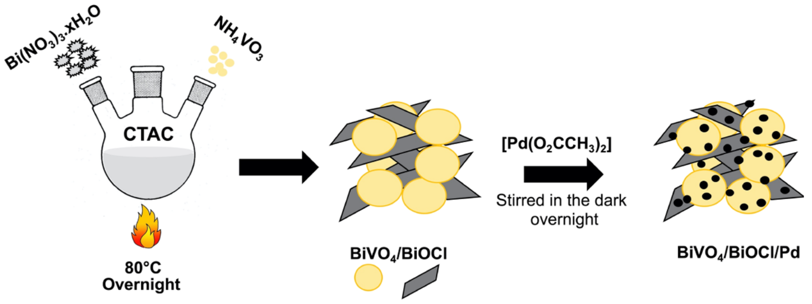

components.[25] These heterojunctions can efficiently separate electron−hole pairs leading to enhanced photocatalytic efficiency.[26−28]

Bismuth oxyhalides (BiOX, X = Cl, Br, I) are unique materials to form heterojunctions with $BiVO_4$ because of their optical properties and hierarchical structure.[29−33] The structure and composition of these unique layered materials promotes electron−hole transfer.[34,35] The band gaps of $BiVO_4$ and BiOX are suited to form a type II p−n heterojunction.[35] In this regard, Song *et al.* have reported enhanced photocatalytic activity of $BiVO_4$/BiOCl for the degradation of methyl orange under visible light irradiation.[36] Chen *et al.* also demonstrated enhanced degradation of methyl orange, RhB, and acid orange II using $BiVO_4$/BiOCl.[37] Ju *et al.* reported a $BiVO_4$/BiOI heterojunction with a flower-like structure for the decomposition of MB dye, which also had antimicrobial activity toward *Pseudomonas aeruginosa*.[38] Chen *et al.* prepared core@shell hierarchical mesoporous $BiVO_4$/BiOBr spindles for the degradation of RhB and norfloxacin antibiotic.[39] Although these materials exhibited higher photocatalytic reactivity upon the addition of BiOX, the composites were prepared in a two-step method. This required the preparation of $BiVO_4$ first, followed by BiOX incorporation. While this approach results in the anticipated materials, preparing both structures simultaneously in a single pot could be advantageous.

To further enhance the photocatalytic reactivity of semiconductor photocatalysts, noble metal nanoparticle surface decoration has been exploited.[40] This enhancement in the reactivity arises when the noble metal's Fermi level is at equilibrium with the conduction band (CB) of the metal oxide and facilitates excited electron transfer while inhibiting charge recombination.[41] Such effects are highly important where charge recombination is a significant issue that leads to diminished photocatalytic reactivity. For instance, our team has demonstrated the role of Pd nanodomains in enhancing the photocatalytic reactivity of $BiVO_4$/BiOBr in the degradation of RhB and the chlorinated biphenyl congener PCB3.[41] In a separate work, Lee *et al.* reported Ag-decorated $BiVO_4$/BiOBr for the degradation of malachite green dye.[40] As such, the generation of the ternary composite structure could be optimal for photocatalytic reactivity; however, the effects of composition and synthetic method remain unclear for $BiVO_4$/BiOX/noble metal materials that could be important for sustainable environmental remediation using visible light.

In this study, we demonstrate a universal one-pot surfactant-assisted route for the synthesis of nanoscale $BiVO_4$/BiOX at relatively low temperatures (Scheme 1). Generating the two metal oxide components simultaneously minimizes the amount of materials required for synthesis, enhancing the synthetic efficiency and maximizing the interactions between the two components of the heterojunction. The effect of the halide identity on the material composition, structure, and photocatalytic properties was explored across Cl, Br, and I.[41] To enhance the charge carrier separation, the surface of the heterojunction catalyst was coated with Pd^0 nanoparticles (Scheme 1). The nanomaterials were extensively characterized using scanning electron microscopy (SEM), transmission electron microscopy (TEM), energy-dispersive spectroscopy (EDS), X-ray diffraction (XRD), X-ray photoelectron spectroscopy (XPS), and UV−vis spectroscopy to verify the composition, structure, and arrangement of the multicomponent materials. Once fully characterized, the photocatalytic reactivity of the materials was explored *via* the degradation of RhB in deionized water as a model organic pollutant. The reactivity was also processed in environmental water samples, including both brackish and salt water, collected from different locations in South Florida, to examine the ability of the photocatalytic materials to drive remediation reactions in environmentally relevant systems. Taken together, our results demonstrate that the ternary composites of $BiVO_4$/BiOX/Pd are highly reactive based upon their multicomponent structure with optimal reactivity arising from $BiVO_4$/BiOBr/Pd. The materials displayed reactivity in all of the selected environmental samples; however, brackish water resulted in diminished reactivity as compared to saltwater environments. Such results demonstrate the potential of photocatalytic materials for use as sustainable systems for remediation where the final composition can be tuned at the atomic level to optimize reactivity under real world conditions.

■ MATERIALS AND METHODS

Chemicals. Bismuth(III) nitrate hydrate, ammonium metavanadate, cetyltrimethylammonium chloride (CTAC), and RhB were purchased from Alfa Aesar. Palladium(II) acetate was purchased from STREM Chemicals, while potassium iodide, and cetyltrimethylammonium bromide (CTAB) were from Sigma. Ethanol (200 proof) was acquired from Pharmco-Aaper. All chemicals were used as received. High purity deionized water (18.2 MΩ·cm) was used for all experiments, unless otherwise noted. For environmental water samples, the samples were collected at the indicated location and used without purification.

Synthesis of the $BiVO_4$/BiOX Heterojunction Catalyst. The single pot synthesis of *m*-$BiVO_4$/BiOX materials was processed using previously published protocols, but adapted for compositions with different halides.[32,41] The synthesis of $BiVO_4$/BiOCl is described; however, changes in the halogen identity in the surfactant were used to generate $BiVO_4$/BiOBr and $BiVO_4$/BiOI. For the synthesis of $BiVO_4$/BiOCl, first, stock solutions of NH_4VO_3 and $Bi(NO_3)_3$ were prepared. In this regard, 117 mg of NH_4VO_3 was added to 10 mL of water at 90 °C, which was stirred vigorously for 10 min and then

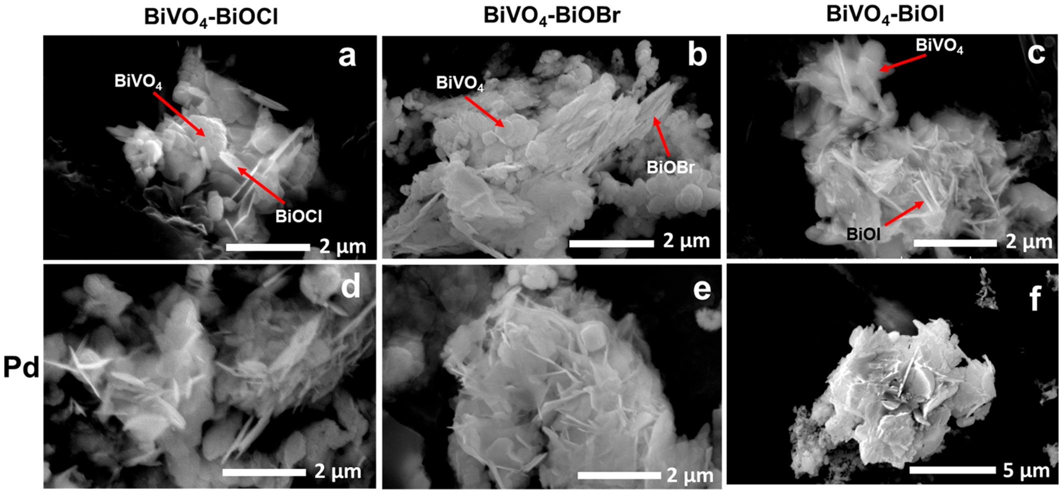

Figure 1. SEM analysis of the (a) $BiVO_4$/BiOCl, (b) $BiVO_4$/BiOBr, (c) $BiVO_4$/BiOI, (d) $BiVO_4$/BiOCl/Pd, (e) $BiVO_4$/BiOBr/Pd, and (f) $BiVO_4$/BiOI/Pd materials.

cooled to room temperature. For the $Bi(NO_3)_3$ stock solution, 970 mg of the hydrate compound was added to 10 mL of water and stirred at room temperature for 15 min, resulting in the production of a white suspension. To generate the heterojunction material, a three-neck round bottom flask was used in which 0.05 M aqueous CTAC was added to 20 mL of water under vigorous stirring for 5 min at 60 °C. Subsequently, the NH_4VO_3 stock solution was added dropwise to the CTAC, followed by the dropwise addition of the $Bi(NO_3)_3$ stock. After all compounds were added, a mustard yellow mixture was obtained, which was left to heat at 80 °C overnight. After reaction, the resulting precipitate was washed with water and ethanol, and then dried in a 60 °C vacuum oven overnight. The exact same procedures were employed to generate $BiVO_4$/BiOI; however, cetyltrimethylammonium iodide (CTAI—see below) was employed as the surfactant.

Synthesis of CTAI. CTAI was synthesized following a method similar to a previously published approach.[42] To achieve this, 500 mL of 60 mM aqueous KI was slowly added to 500 mL of 10 mM aqueous CTAB at room temperature while stirring vigorously. A white precipitate was subsequently formed. The CTAI precipitate was filtered and washed three times with water, and then dried in a 60 °C vacuum oven overnight. The white crystals were then dissolved in acetone and evaporated overnight. Electrospray ionization mass spectrometry was used to confirm the formation of CTAI.

Palladium Deposition. To deposit Pd on the surface of the oxide materials, 100 mg of prepared *m*-$BiVO_4$/BiOX was dispersed in 75 mL of ethanol and then sonicated for 1 min. To this mixture, 8.0 mg of palladium(II) acetate was added, and the solution was sonicated for 30 s. The solution was left to stir overnight in the dark, after which the materials were washed three times with ethanol and dried in a vacuum oven overnight at 60 °C.

Photocatalytic Experiments. The photocatalytic experiments were carried out on a Sol 1A Class ABB 94061A solar simulator (Newport Corporation, USA) with 100 mW/cm^2 power output produced by a 1000 W Xenon-Mercury lamp. The distance between the light source and the top of the reaction solution was ~15 cm. The photocatalytic activity of various catalysts was evaluated by observing the degradation of RhB dye as a model organic pollutant. In a typical experiment, 20 mg of the photocatalyst was dispersed in 18 mL of water, followed by the addition of 2 mL of the RhB dye solution [100 mg/L in deionized (DI) water], which was added in the dark. This resulted in a final reaction RhB concentration of 10 mg/L. The solution was left to stir in the dark for 30 s, after which it was irradiated by the solar simulator. At selected time intervals, 600 µL aliquots were taken and centrifuged to remove the catalyst particles. UV−vis spectroscopy was then used to quantify the RhB concentration in the reaction to monitor the dye degradation process.

Characterization. Crystallographic data were obtained for all photocatalyst samples on a Philips MRD X'Pert X-ray diffractometer using Cu Kα radiation. SEM images were obtained on an FEI XL-30 microscope operating at 20 kV. SEM samples were prepared by dispersing the $BiVO_4$/BiOX materials in ethanol and dropcasting 15 µL onto an aluminum stub. TEM was performed with a JEOL JEM-1400 system operating at 80 kV, while dark-field STEM images were completed using a Tecnai F30 by FEI operating at 300 kV. EDS analysis was conducted employing an Octane Optima T-60 detector (EDAX). For all TEM analyses, the samples were prepared by dropcasting 4 µL of the dispersed sample in ethanol onto a TEM grid. The samples were allowed to dry completely in a desiccator. XPS characterization was obtained using a PHI 5000 Versa Probe II equipped with a focused monochromatic Al Kα source. The detection of the recombination and lifetime of photogenerated charges of nanomaterials was performed by using a steady-state/Transient fluorescence spectrometer (Edinburgh/FL920) equipped with a Ge detector. Elemental analysis of the materials was performed using an Agilent 7900 inductively coupled plasma mass spectrometer (ICP−MS). Total organic carbon (TOC) analysis was performed on a Shimadzu TOC-L CPH. Finally, all UV−vis absorption spectra were recorded on a Shimadzu UV-2600 spectrophotometer.

■ RESULTS AND DISCUSSION

Material Synthesis. The synthesis of the $BiVO_4$/BiOX composite materials was achieved using a unique one-pot approach previously designed for the generation of $BiVO_4$/BiOBr but expanded for the production of the chloride and iodide variants (Scheme 1).[41] Typical approaches for the generation of such materials commonly requires the production of the $BiVO_4$ and BiOX separately, followed by their combination. The production of the materials in a single pot allows for a greater integration between the two components, which has been proven to be important for the photocatalytic properties.[41] The production of $BiVO_4$/BiOX was achieved by mixing NH_4VO_3 with excess $Bi(NO_3)_3{\cdot}5H_2O$ in aqueous solution followed by the addition of CTAC, CTAB, or CTAI to prepare $BiVO_4$/BiOCl, $BiVO_4$/BiOBr, or $BiVO_4$/BiOI, respectively. Excess $Bi(NO_3)_3$ is necessary to facilitate the formation of the nanosheets of the BiOX composite.[41] Note that because CTAI is not readily commercially available, it was prepared in house prior to use *via* a halogen substitution reaction. To enhance the photocatalytic activity of the heterojunction composites, Pd nanoparticles were deposited on the surfaces of the oxide materials. This was achieved by dispersing the $BiVO_4$/BiOX and $Pd(CH_3COO)_2$ in ethanol while stirring in the dark overnight. This results in the deposition of Pd nanoparticles on the material surface (*vide infra*), where the Pd-coated structures were green in color.

The initial characterization of the materials before and after Pd nanoparticle surface decoration focused on the use of electron microscopy. Figure 1 presents SEM images of the materials as a function of halogen identity and Pd incorporation. For the Pd-free samples (Figure 1a−c), two morphologies were evident in each sample: a solid 3D/cracked material for the $BiVO_4$ component and a plate-like morphology for the various BiOX structures. Specifically, for the $BiVO_4$/BiOCl materials, the $BiVO_4$ structure had an average diameter of 0.7 ± 0.4 μm, while the BiOCl component had an average width of 0.7 ± 0.3 μm and an average thickness of 0.06 ± 0.02 μm. When considering the $BiVO_4$/BiOBr system, the $BiVO_4$ material was 0.6 ± 0.4 μm in diameter, whereas the BiOBr nanoplates were 1.0 ± 0.5 μm wide and 0.1 ± 0.06 μm thick. Finally, $BiVO_4$/BiOI samples was also composed of BiOI nanoplates with an average width of 0.6 ± 0.3 μm and average thickness of 0.07 ± 0.04 μm. This sample also contained a $BiVO_4$ component with an average diameter of 2.6 ± 0.9 μm. No substantial change in the material morphology was evident; however, the dimensions of the different structures did vary as a function of the halogen present in the BiOX sample. After deposition of the Pd nanoparticles onto the oxide surface (Figure 1d−f), the material morphology remained the same, as observed by SEM. Note that the Pd nanoparticles could not be observed *via* SEM, indicating that these components were quite small, as anticipated.

TEM analysis of the same materials is also performed to access a more complete understanding of the material structure, as shown in Figure 2. For the $BiVO_4$/BiOCl/Pd materials (Figure 2a), the sample appears to be a mixture of plate-like structures with rounded edges, consistent with the SEM images. Analysis of the $BiVO_4$/BiOBr/Pd materials is presented in Figure 2b. For this sample, the transparent plate-like structures are the BiOBr nanoplates while the darker components are $BiVO_4$, consistent with our prior studies.[41] Finally, for the $BiVO_4$/BiOI materials, again plate-like materials were observed; however, the edges of the samples were quite jagged. This suggests that while the plate morphology for the BiOX component is preserved, regardless of the halogen identity, the halide identity does play an important role in controlling the edge structure (rounded *vs* jagged). In all three samples, the deposition of nanoscale Pd particles onto the $BiVO_4$/BiOX is observed as small spheres ubiquitously deposited throughout the structures. The average Pd nanoparticle size was 20 ± 7 nm (n = 100 particles) in diameter. To identify the overall composition of the materials, ICP−MS analysis was conducted (Supporting Information, Figure S1), which revealed the Pd loadings in the materials were 1.7, 2.9, and 3.0 wt % Pd for the $BiVO_4$/BiOBr/Pd, $BiVO_4$/BiOCl/Pd, and $BiVO_4$/BiOI/Pd structures, respectively. In addition, this analysis indicates that the $BiVO_4$/BiOX ratio for the Cl^-, Br^-, and I^- based materials was quite similar with values of 1.6, 1.3, and 1.0. For the BiOBr/BiOCl/Pd structures obtained after calcination (*vide infra*), the $BiVO_4$/BiOBr ratio was 1.2.

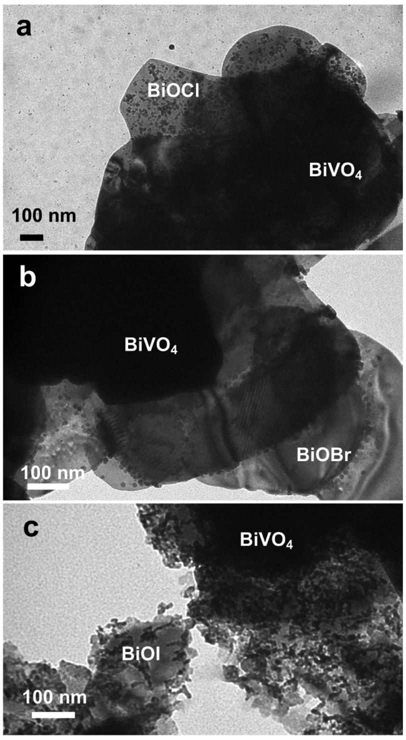

Figure 2. TEM analysis of the (a) $BiVO_4$/BiOCl/Pd, (b) $BiVO_4$/BiOBr/Pd, and (c) $BiVO_4$/BiOI/Pd materials.

To confirm the composition and the arrangement of the heterojunction in the composite materials, dark-field STEM images were obtained along with EDS elemental mapping. Figure 3 shows the results for the $BiVO_4$/BiOI/Pd materials, while the analysis of the $BiVO_4$/BiOCl/Pd materials is shown in the Supporting Information (Figure S2). As shown in Figure 3a, a dark field STEM image of the $BiVO_4$/BiOI/Pd heterojunction is presented, where the highlighted region (orange square) was analyzed *via* EDS mapping. Figure 3b−d highlights the regions where Bi, V, and I are present in the sample, respectively, arising from the $BiVO_4$ and BiOI components of the sample. As is evident, a close interconnection between the two oxide systems is present, consistent with heterojunction formation. Mapping of the Pd component is shown in Figure 3e, where the noble metal nanoparticles demonstrated deposition on both of the oxide surfaces. Such results were anticipated based upon the synthetic method and were consistent with our previous $BiVO_4$/BiOBr/Pd system.[41] Similar results were obtained for the EDS mapping of the $BiVO_4$/BiOCl/Pd materials with uniform Pd deposition on both the $BiVO_4$ and BiOCl components.

Figure 4a presents powder XRD patterns for the m-$BiVO_4$/BiOCl/Pd and m-$BiVO_4$/BiOI/Pd materials. XRD analysis on the m-$BiVO_4$/BiOBr/Pd sample, confirming its composition, was reported in a prior work.[41] For both of the present samples, monoclinic scheelite m-$BiVO_4$ is evidenced by reflections at 2θ = 28.7, 30.5, 34.2, and 34.9° (JCPDS 14-0688). For the BiOCl system (black plot), additional reflections observed at 2θ = 25.8, 32.4, 33.4, and 46.5° are consistent with tetragonal BiOCl (JCPDS 06-0249), and similarly for the BiOI system, where the additional reflections occur at 2θ = 29.8, 31.7, and 45.5° (JCPDS 73-2062). For both samples, no diffraction peaks associated with the Pd component were observed, consistent with their low concentration with respect to the m-$BiVO_4$/BiOX components.

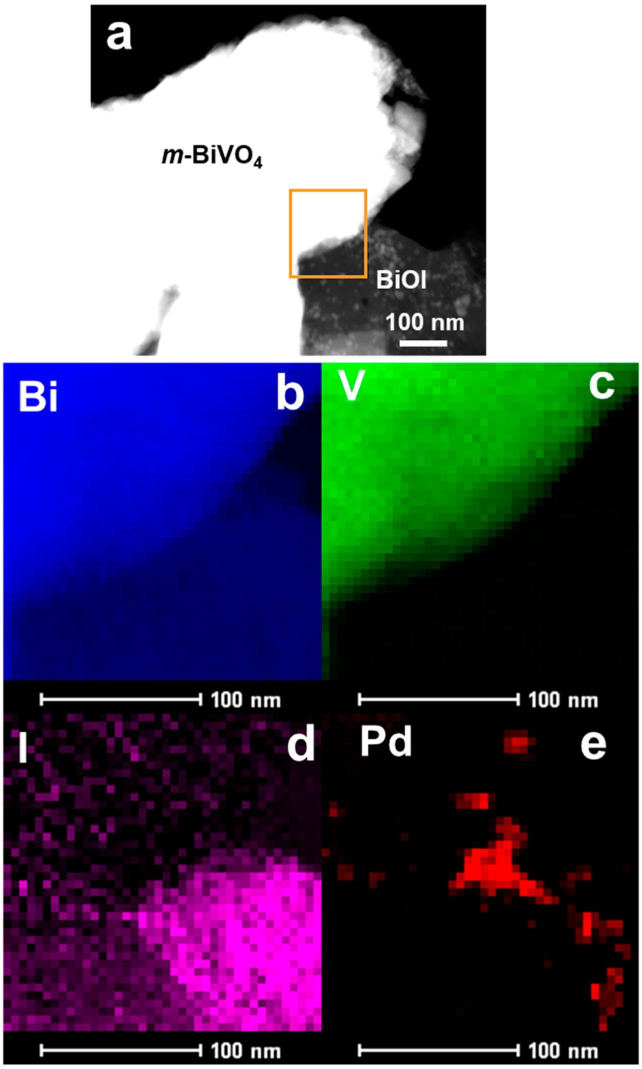

Figure 3. High-angle annular dark-field scanning transmission electron microscopy and EDS mapping analysis of the BiVO$_4$/BiOI/Pd materials. Part (a) presents the STEM image where EDS mapping of the region in the orange box is shown for (b) Bi, (c) V, (d) I, and (e) Pd.

The surface composition of the materials is also analyzed by XPS, as shown in Figure 4b−f. Based on the analysis, Bi, V, Cl, and Pd were present in the BiVO$_4$/BiOCl/Pd composite, while Bi, V, I, and Pd were present in the BiVO$_4$/BiOI/Pd samples. As shown in Figure 4b specifically, peaks at 159.0 and 164.5 eV for Bi 4f$_{7/2}$ and Bi 4f$_{5/2}$, respectively, confirm the presence of Bi^{3+} in BiVO$_4$/BiOCl and BiVO$_4$/BiOI. Figure 4c demonstrates the presence of V^{5+} in both BiVO$_4$-based samples with peaks at 516.7 eV for V 2p$_{3/2}$ and 524.4 eV for V 2p$_{1/2}$. For the BiVO$_4$/BiOCl sample, Cl$^-$ was confirmed with a Cl 2p$_{3/2}$ peak at 198.2 eV (Figure 4d). In addition, Figure 4e presents the I 3d$_{5/2}$ and I 3d$_{3/2}$ peaks at 618.9 and 630.6 eV, respectively, arising from I$^-$ for BiVO$_4$/BiOI. Finally, Figure 4f presents the XPS analysis for the Pd component in the heterostructured materials. Peak deconvolution was employed to identify the composition of the metallic component, which indicated that Pd^0 and PdO were present in both BiVO$_4$/BiOCl/Pd and BiVO$_4$/BiOI/Pd. This is evidenced by peaks at 335.7 and 341.0 eV for Pd 3d$_{5/2}$ and Pd 3d$_{3/2}$, respectively, arising from Pd^0, while PdO peaks were noted at 336.8 eV (Pd 3d$_{5/2}$) and 342 eV (Pd 3d$_{3/2}$). From this deconvolution analysis, 91.8% of the palladium in the sample was Pd^0 while 8.2% was PdO. XPS analysis of the BiVO$_4$/BiOBr/Pd materials was reported previously, confirming its composition.[41]

Figure S3 in the Supporting Information presents the UV−vis DRS spectra of all three composites. All of the catalysts exhibited dual absorption edges indicating the presence of two species, as anticipated. BiVO$_4$/BiOCl, BiVO$_4$/BiOBr, and BiVO$_4$/BiOI presented absorption edges around 504/387, 508/516, and 517/459 nm, respectively. The band gap (E_g) values of the materials were estimated to be 2.46/3.20, 2.44/2.40, and 2.40/2.70 eV for BiVO$_4$/BiOCl, BiVO$_4$/BiOBr, and BiVO$_4$/BiOI, respectively. Such results are consistent with previous reports.[37,43]

Taken together, the characterization analysis confirms the formation of the BiVO$_4$/BiOX materials using a single pot approach. Selection of the halogen identity was controlled by the surfactant composition, allowing for a direct and facile synthesis where the incorporation of the Pd nanoparticle cocatalysts was achieved regardless of the oxide composition. This approach allows for the production of similar structures with only minor morphology and size differences based upon the BiOX composition. Such similarities are important to allow for direct photocatalytic reactivity comparisons to identify optimal heterojunction compositions and arrangements for long-term and sustainable photocatalytic degradation of environmental pollutants.

Photocatalytic Activity. The photocatalytic activities of the Pd-free and Pd particle-decorated BiVO$_4$/BiOX samples were evaluated by following the degradation of the RhB dye. RhB is considered a model organic pollutant where its degradation kinetics can be used to elucidate the photocatalytic properties of the catalyst using a readily accessible reaction. Studies of both systems (with and without Pd) are important to identify the changes in the material photocatalytic reactivity based upon both the heterojunction composition and Pd nanoparticle surface decoration. For this reaction, 20.0 mg of the catalyst was dispersed in 20 mL of 10 mg/L RhB dye in water. After 30 s of stirring in the dark, the reaction was illuminated under a solar simulator from which 600 μL aliquots were extracted at select time intervals. Such a short incubation time prior to irradiation was selected as no change in the dye concentration was observed even after 30 min in the dark indicating that the dye does not show any appreciable adsorption on the catalyst (Supporting Information, Figure S4).[41] The photocatalytic experiments were carried out on a solar simulator with a 100 mW/cm^2 power output produced by a 1000 W Xenon-Mercury lamp with a wavelength range of 200−2500 nm. The distance between the light source and the top of the reaction solution was ∼15 cm. To quantify the reaction progress, UV−vis spectroscopy was employed based upon the absorbance of the RhB substrate. From this analysis, the progression of the reaction as a function of time can be monitored, and the actual rate constants (k_{obs}) of the photocatalytic process can be extracted.

Figure 5a shows the photodegradation of the dye as a function of irradiation time for all six samples. For the Pd-free photocatalysts, the RhB dye was completely degraded in <10 min for BiVO$_4$/BiOCl and BiVO$_4$/BiOBr; however, only 92% of RhB was degraded after 70 min when BiVO$_4$/BiOI was driving the reaction. From these data, the rate constants were determined (Figure 5b), giving rise to k_{obs} values of 0.54 ± 0.07 min^{-1} for BiVO$_4$/BiOCl, 0.49 ± 0.06 min^{-1} for

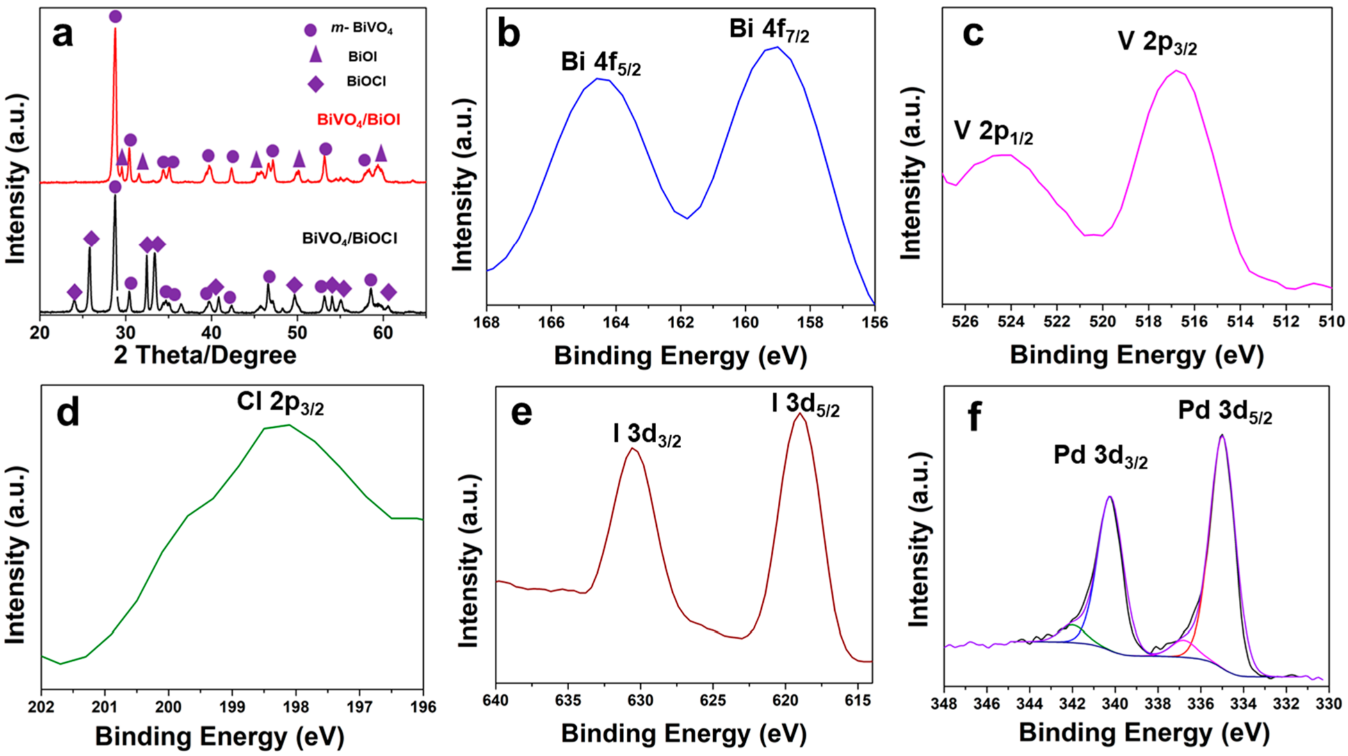

Figure 4. X-ray-based characterization of $BiVO_4$/BiOCl/Pd and $BiVO_4$/BiOI/Pd materials. Part (a) presents the XRD diffraction pattern for both systems, while parts (b−f) display the XPS measurements for the (b) Bi, (c) V, (d) Cl, (e) I, and (f) Pd components.

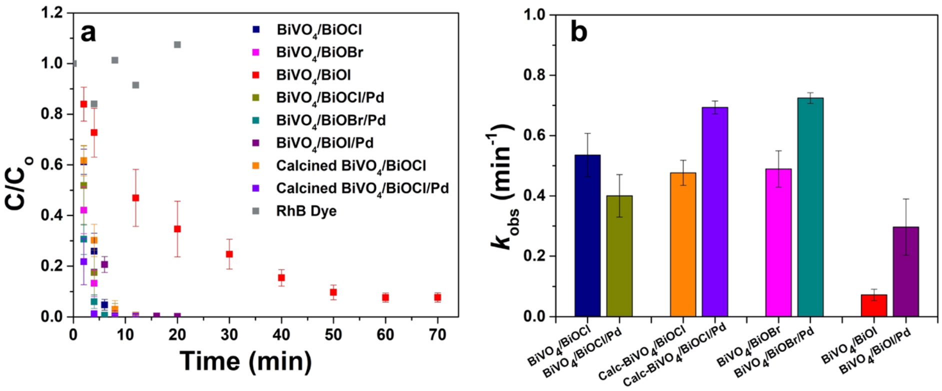

Figure 5. Photocatalytic analysis for the degradation of RhB. Part (a) presents the reaction analysis as a function of time, while part (b) displays the rate constants for the individual photocatalysts.

$BiVO_4$/BiOBr, and 0.07 ± 0.02 min^{-1} for $BiVO_4$/BiOI. Notable changes in these values were observed when the materials were decorated using the noble metal nanoparticle cocatalysts. In this regard, for the $BiVO_4$/BiOCl/Pd, $BiVO_4$/BiOBr/Pd, and $BiVO_4$/BiOI/Pd materials, rapid RhB degradation was noted, resulting in k_{obs} values of 0.40 ± 0.07, 0.72 ± 0.02, and 0.30 ± 0.09 min^{-1}, respectively. As a control, the same reaction was studied using just the parent $BiVO_4$ materials. Using this structure, significantly diminished reactivity was observed, giving rise to a notably lower k_{obs} value of 0.03 ± 0.001 min^{-1}.

To measure the removal efficiency of the photocatalysts, TOC analysis was performed on RhB dye before and after degradation. Figure S5 in the Supporting Information shows the percent of organic carbon mineralized after RhB degradation using the photocatalytic materials. In this analysis, 13.3, 35.2, and 4.4% of the dye were mineralized using the calcined $BiVO_4$/BiOCl/Pd, $BiVO_4$/BiOBr/Pd, and $BiVO_4$/BiOI/Pd photocatalysts, respectively. These results, in combination with the UV−vis analysis, suggest that while the first reaction step for RhB degradation is similar for the calcined $BiVO_4$/BiOCl/Pd and $BiVO_4$/BiOBr/Pd materials, the $BiVO_4$/BiOBr/Pd demonstrated a greater degree of organic mineralization.

When comparing the rate constants for the reactions, two specific observations are noteworthy. First, for the Pd-free materials, the $BiVO_4$/BiOCl and $BiVO_4$/BiOBr samples presented very similar k_{obs} values; however, for the $BiVO_4$/BiOI system, the rate constant was substantially diminished. The lower reactivity for the $BiVO_4$/BiOI materials likely arises from the ability of BiOI to exhibit n-type behavior because of its large electron affinity of 5.2 eV, which is consistent with n-type semiconductors.[44] Second, the k_{obs} values generally increased when the Pd nanoparticle co-catalysts were added

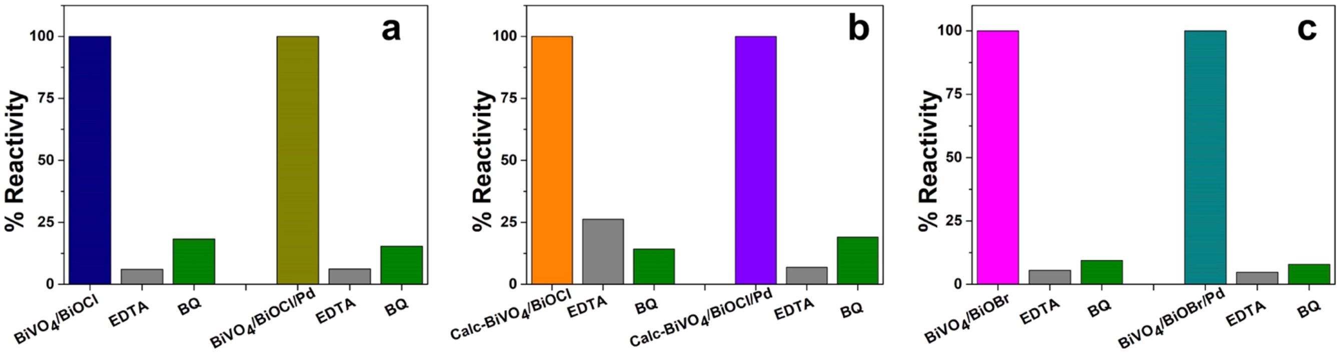

Figure 6. Scavenger analysis for the (a) $BiVO_4$/BiOCl/Pd, (b) calcined $BiVO_4$/BiOCl/Pd, and (c) $BiVO_4$/BiOBr/Pd systems.

to the system. This was evident for the $BiVO_4$/BiOBr and $BiVO_4$/BiOI materials, which increased by 47 and 313%, respectively. Such events arise from the electrons in the excited system transferring into the metallic material, which prevents charge recombination and diminished reactivity. This effect was substantial in $BiVO_4$/BiOI because of the high recombination rate of the Pd-free materials. Interestingly, the $BiVO_4$/BiOCl/Pd materials demonstrated lower photocatalytic reactivity as compared to the $BiVO_4$/BiOCl structures, which was quite unanticipated.

Clear differences in the photocatalytic reactivity of the $BiVO_4$/BiOI-based materials were evident, as compared to the other structures, which might be attributed to high rates of charge recombination. To measure this effect, the intermittent photocurrent response was measured to evaluate the interfacial charge separation between the $BiVO_4$/BiOX samples with and without light irradiation every 10 s. As anticipated, $BiVO_4$/BiOBr/Pd showed the highest photocurrent value compared to the other materials, while $BiVO_4$/BiOI showed the lowest photocurrent generation (Supporting Information, Figure S6a). Electrochemical impedance spectra (EIS) were also used to obtain information on charge transfer resistance of the samples. In this test, the smaller the diameter of the semicircle, the lesser the resistance, demonstrating a faster charge transfer rate. In Figure S6 of the Supporting Information, $BiVO_4$/BiOBr/Pd shows the fastest charge transfer rate, followed by calcined $BiVO_4$/BiOCl/Pd > calcined $BiVO_4$/BiOCl > $BiVO_4$/BiOBr > $BiVO_4$/BiOI/Pd > $BiVO_4$/BiOI. In both measurements, the iodine-based materials confirmed rapid charge recombination, consistent with the observed diminished photocatalytic reactivity.

To further elucidate a structural basis for the diminished reactivity for $BiVO_4$/BiOCl/Pd as compared to the parent $BiVO_4$/BiOCl, the effects of surface material defects were examined. Wei and colleagues have shown previously that Au/TiO_2 materials that possessed oxygen vacancies at the interface led to diminished catalytic reactivity compared to the corresponding defect-free material.[45] The researchers calcined the materials to remove these defects, which led to enhanced CO oxidation capabilities. To examine if such surface defects may be present in the $BiVO_4$/BiOCl materials, the structures were calcined at 320 °C for 3 h, followed by Pd nanoparticle deposition using the standard method. The calcined $BiVO_4$/BiOCl and $BiVO_4$/BiOCl/Pd materials were then used to drive photocatalytic RhB degradation, where complete substrate consumption was observed in <10 min with rate constants of 0.48 ± 0.04 min^{-1} for $BiVO_4$/BiOCl and 0.69 ± 0.02 min^{-1} for $BiVO_4$/BiOCl/Pd (Figure 5b). The values for the original and calcined $BiVO_4$/BiOCl structures were quite similar; however, substantially increased reactivity was noted for the calcined Pd-containing structures ($BiVO_4$/BiOCl/Pd), as anticipated. This suggests that defects at the oxide surface are responsible for the diminished reactivity for the uncalcined $BiVO_4$/BiOCl/Pd materials. Previous studies by Wei and colleagues[45] suggest that oxygen vacancies may be the main source of these defects; however, additional detailed analyses of the metal/oxide interface are required to fully identify the defects present.

The recyclability of the calcined $BiVO_4$/BiOCl/Pd was evaluated over three degradation experiments using the RhB dye. After each reaction cycle, the particles were collected and washed with DI water followed by ultrasonication to properly disperse the particles in the new reaction mixture. As shown in the Supporting Information, Figure S7, 100% of the dye was degraded in all three cycles within 12 min indicating that the catalysts retained their activity over multiple catalytic cycles without diminished reactivity. In addition, SEM analysis of the $BiVO_4$/BiOCl/Pd particles after one catalytic cycle demonstrated negligible structural changes, suggesting that the materials were generally photostable (Supporting Information, Figure S7). Such stability is consistent with the observed recyclability of the materials.

To probe the active species in the reaction, charge carrier scavengers were employed for the $BiVO_4$/BiOCl and $BiVO_4$/BiOBr systems as they were substantially more reactive than the $BiVO_4$/BiOI structures. For all of the materials, the photocatalytic reactions were studied in the presence of ethylenediaminetetraacetic acid (EDTA) to scavenge holes (h^+) and benzoquinone (BQ) to scavenge superoxide radicals ($^{\bullet}O_2^-$). These two species are the most likely to drive the observed photodegradation processes through redox reactions with the RhB substrate. Figure 6a presents the scavenger analysis specifically for the uncalcined $BiVO_4$/BiOCl structures, where the k_{obs} values are compared for the materials both with and without Pd nanoparticle decoration. For the $BiVO_4$/BiOCl-driven process in the presence of EDTA and BQ, the k_{obs} values decreased by 93.9 and 81.7%, respectively, as compared to the standard reaction. For the uncalcined $BiVO_4$/BiOCl/Pd-based reactions, nearly identical results were observed as compared to the Pd-free materials, with a 93.8% decrease in reactivity for the EDTA-scavenged reaction and 84.7% decrease for the reactivity in the presence of BQ. For the calcined $BiVO_4$/BiOCl and $BiVO_4$/BiOCl/Pd materials, similar trends as compared to the uncalcined materials were observed (Figure 6b). The major difference arises from the BQ-scavenged reactions using the calcined $BiVO_4$/BiOCl, which demonstrated a greater impact on the reactivity as compared to the EDTA system, suggesting the role of oxygen vacancies in the uncalcined material in scavenging the excited electrons. While such a difference was observed in both cases, the presence of EDTA and BQ resulted in substantial reactivity decreases, suggesting that both h^+ and $^{\bullet}O_2^-$ are key reaction species driving the degradation of RhB.

When the $BiVO_4$/BiOBr-based materials were studied in the presence of the scavengers, similar reactivity effects were noted as compared to the $BiVO_4$/BiOCl system. To this end, for the Pd-free $BiVO_4$/BiOBr materials, the presence of EDTA led to a 94.4% reactivity decrease, while BQ diminished the reactivity by 90.5%. For the more reactive $BiVO_4$/BiOBr/Pd, EDTA and BQ again scavenged the reaction, resulting in reactivity decreases of 95.2 and 92.1%, respectively. Based upon the scavenger data, it is evident that both h^+ and $^{\bullet}O_2^-$ are key reaction species driving the photocatalytic degradation of RhB. In nearly all cases, the EDTA demonstrated greater reactivity decreases as compared to the systems with BQ, suggesting that h^+ play a larger role in the photocatalytic degradation reaction.

Scheme 2. **Proposed Photocatalytic Mechanism for the $BiVO_4$/BiOX/Pd Materials Under Optical Illumination**[a]

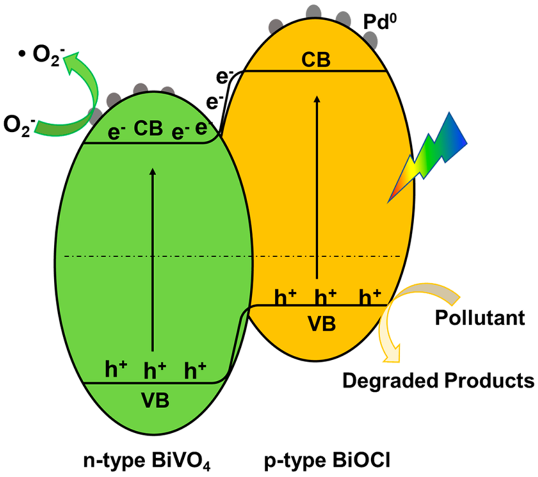

[a] Note that formation of $^{\bullet}O_2^-$ facilitates RhB degradation.

From the reaction analyses discussed above, a possible pathway for the degradation of RhB with the $BiVO_4$/BiOX materials can be described (Scheme 2). For the $BiVO_4$/BiOCl materials, a p−n heterojunction is formed between n-type $BiVO_4$ and p-type BiOCl, resulting in the generation of an internal static electric field, and as electrons are transferred between both materials, their Fermi levels equilibrate. As a result, the space charge region at the interface causes the bands of the n-type and p-type materials to bend.[36] From this, the charge transfer between the two components is completed within picoseconds, which is faster than the lifetime of an electron−hole pair on a single semiconductor (nanoseconds).[46] As such, the heterojunction results in enhanced reactivity as compared to the single component materials. When the composite is irradiated with light, both $BiVO_4$ and BiOCl are activated and the excited electrons transfer from the valence band of BiOCl to its CB then to the CB of $BiVO_4$ leaving reactive holes in BiOCl which oxidize the pollutant. The electrons from $BiVO_4$ react with dissolved oxygen to form superoxide radicals, which also degrade the pollutant. However, upon addition of Pd^0 particles on the surface of $BiVO_4$/BiOCl, there was no enhancement in the photocatalytic degradation of RhB.[41] This potentially arises from oxygen vacancies on the oxide surface, which could trap the electrons to prevent their transfer to metallic Pd.[45] This was supported by calcination to remove these defects, resulting in $BiVO_4$/BiOCl/Pd with enhanced reactivity, as anticipated.

Similar effects are anticipated for the $BiVO_4$/BiOBr/Pd and $BiVO_4$/BiOI/Pd materials, as previously described for $BiVO_4$/BiOBr/Pd.[41] For $BiVO_4$/BiOI, both materials can be excited under visible light. $BiVO_4$ has a band gap of approximately 2.4 eV, while BiOI has a band gap of approximately 2.7 eV. Similar to $BiVO_4$/BiOCl, a p−n heterojunction was formed upon contact until the Fermi levels are equilibrated in which a built-in potential is formed across the junction.[30] When the material is illuminated with solar light, electrons accumulate onto the CB on $BiVO_4$, while holes accumulate on BiOI, which are both responsible for the degradation of RhB. When coated with Pd^0 particles, an enhancement in the reactivity is observed because the Pd particles facilitate the transfer of excited electrons to form superoxide radicals.

When considering the reactivity of the present materials with comparable structures, enhanced reactivity is noted from the single pot heterostructures prepared at low temperatures. For instance, Lv *et al.* employed a one-pot synthetic method for the production of $BiVO_4$/BiOCl; however, significantly higher temperatures were used during the synthesis (300 °C).[47] From this approach, flower-like nanoplates were prepared and subsequently used to degrade RhB. Using these materials, a notably longer reaction time was required to degrade RhB as compared to the present structures (180 *vs* 8 min). In a separate work, Huang *et al.* synthesized $BiVO_4$/BiOI using a two-pot approach. In this case, they were able to examine the effect of using different ratios of $BiVO_4$/BiOI in the composite,[31] where they demonstrated a maximum reactivity of 97% RhB degradation in 3 h. Such a reaction time is longer than those required using the single pot prepared $BiVO_4$/BiOI materials with and without Pd of the present study, which are 12 and 70 min, respectively.

While the photocatalytic reactivity of the $BiVO_4$/BiOX materials varies as a function of composition, an intriguing application of these materials is in the sustainable degradation of environmental pollutants. In this regard, molecular dyes represent prime examples of pollutants that could be degraded using these catalysts; however, changes in the material reactivity may occur based upon the reaction medium. To examine the possibility of exploiting the $BiVO_4$/BiOX-materials for pollutant remediation, the reactivity of one of the most reactive materials, $BiVO_4$/BiOBr/Pd, was processed in water obtained from different environmental samples in Miami-Dade County. Based upon the geographical location, a comparison between the reactivity of the materials in brackish water obtained in canals and lakes, and saltwater from Biscayne Bay and the Atlantic Ocean, was done to elucidate environmental effects on reactivity. For this comparison, five different water samples were chosen: the Everglades, the lake on the North campus of Miami Dade College (MDC), Lake Osceola on the University of Miami campus, Bayfront Park in the city of Miami, and North Beach on Miami Beach. The first three samples are brackish water, while the last two are saltwater samples. TOC analysis was completed on each environmental water sample with values of 120.6 (North Beach), 169.4 (Bayfront Park), 342.8 (MDC North), 341.1 (Lake Osceola),

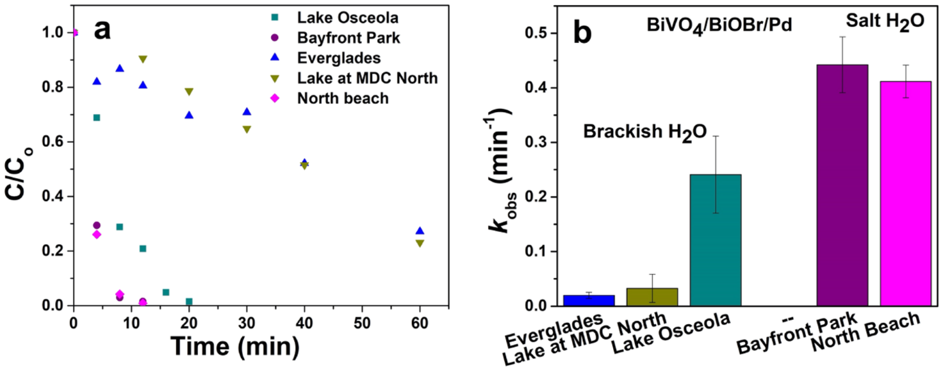

Figure 7. Effects of environmental water samples on the photocatalytic reaction driven using $BiVO_4$/BiOBr/Pd. Part (a) presents the reaction analysis as a function of time, while part (b) displays the rate constants for the individual systems.

and 1486.9 (Everglades) μM. Thus, a range of samples with different TOC concentrations is available to compare the reactivity of the photocatalyst.

For the reactions in the environmental media, all the reaction conditions were the same as described above; however, the deionized water was replaced with the brackish or saltwater samples. This includes the water that the $BiVO_4$/BiOBr/Pd was dispersed in, as well as the water used to prepare the RhB dye stock solution. No pretreatment of the environmental samples was processed to avoid changes in the medium. As shown in Figure 7, the saltwater samples degraded the dye faster than the brackish water, based upon the reaction k_{obs} values. To this end, the fastest reactions were processed in the Bayfront Park and North Beach waters with k_{obs} values of 0.44 ± 0.05 and 0.41 ± 0.03 min^{-1}. These values were slightly lower than the rate constant for the reaction processed in deionized water (0.72 ± 0.02 min^{-1}); however, they are significantly higher than the values for the brackish water samples: 0.02 ± 0.01 min^{-1} for Everglades water, 0.03 ± 0.03 min^{-1} for MDC lake water, and 0.24 ± 0.07 min^{-1} for Lake Osceola water. Even though the reactivity of the materials decreased for every reaction medium, the systems still maintain the ability to degrade the model environmental pollutant, suggesting that the photocatalytic remediation of environmental systems is possible. Interestingly, the samples with the lower TOC generally demonstrated higher k_{obs} values, although no direct correlation between reactivity and TOC values was evident; this suggests that the identity of the dissolved organic matter, not just the total concentration, may differently affect the reactivity.

■ CONCLUSIONS

Herein, we have described a sustainable, low energy one-pot synthetic method for the fabrication of nanosized $BiVO_4$/BiOCl and $BiVO_4$/BiOI heterojunction materials, similar to the synthetic method for $BiVO_4$/BiOBr.[41] In general, the synthetic method produces highly integrated nanomaterials with an intimate heterojunction between the two components. The synthetic approach is readily adapted to any of the BiOX compositions based upon the halide present in the surfactant used in the synthesis, where the final structures were generally comparable between the different BiOX compositions. In addition, the deposition of Pd nanoparticles on the surface of the materials can also be achieved to generate the $BiVO_4$/BiOX/Pd ternary composites. The photocatalytic activity of the materials was sensitive to the halide in the BiOX component, where the $BiVO_4$/BiOCl- and $BiVO_4$/BiOBr-based structures were significantly more reactive than the $BiVO_4$/BiOI-based materials. Interestingly, the $BiVO_4$/BiOCl structures appear to contain oxygen vacancies at the material interface, which resulted in diminished reactivity when Pd nanoparticles were deposited onto the surface. Calcination was employed to remove these vacancies, which significantly increased the photocatalytic reactivity. Finally, the structures were highly reactive in both deionized water and environmentally sourced water samples, strongly suggesting that they could be adapted and exploited for long-term, sustainable remediation of environmental pollutants using sunlight. Such methods are highly attractive as they may alleviate the necessity of catalyst regeneration and secondary reactants (e.g., H_2) for environmental remediation capabilities that limit current methods.

■ ASSOCIATED CONTENT

Supporting Information

The Supporting Information is available free of charge at https://pubs.acs.org/doi/10.1021/acsanm.1c00481.

> ICP/MS, STEM/EDS mapping, UV−vis DRS, photocurrent and EIS spectral analyses, TOC measurements, and recyclability analysis (PDF)

■ AUTHOR INFORMATION

Corresponding Author

Marc R. Knecht − *Department of Chemistry, University of Miami, Coral Gables, Florida 33146, United States; Dr. J.T. Macdonald Foundation Biomedical Nanotechnology Institute, University of Miami, Miami, Florida 33136, United States;* orcid.org/0000-0002-7614-7258; Email: knecht@miami.edu

Authors

Mary O. Olagunju − *Department of Chemistry, University of Miami, Coral Gables, Florida 33146, United States*
Elsayed M. Zahran − *Department of Chemistry, Ball State University, Muncie, Indiana 47306, United States;* orcid.org/0000-0003-3456-515X
Jacqueline M. Reed − *Department of Chemistry, University of Miami, Coral Gables, Florida 33146, United States*
Elnaz Zeynaloo − *Department of Chemistry, University of Miami, Coral Gables, Florida 33146, United States;* orcid.org/0000-0001-7152-5857
Dharmendra Shukla − *Department of Physics, University of Miami, Coral Gables, Florida 33146, United States*

Joshua L. Cohn − *Department of Physics, University of Miami, Coral Gables, Florida 33146, United States;* orcid.org/0000-0002-0702-9872

Bapurao Surnar − *Department of Biochemistry and Molecular Biology, Leonard M. Miller School of Medicine, University of Miami, Miami, Florida 33136, United States;* orcid.org/0000-0001-5997-3120

Shanta Dhar − *Department of Biochemistry and Molecular Biology, Sylvester Comprehensive Cancer Center, Leonard M. Miller School of Medicine, University of Miami, Miami, Florida 33136, United States;* orcid.org/0000-0003-3042-5272

Leonidas G. Bachas − *Department of Chemistry, University of Miami, Coral Gables, Florida 33146, United States; Dr. J.T. Macdonald Foundation Biomedical Nanotechnology Institute, University of Miami, Miami, Florida 33136, United States;* orcid.org/0000-0002-3308-6264

Complete contact information is available at: https://pubs.acs.org/10.1021/acsanm.1c00481

Notes

The authors declare no competing financial interest.

■ ACKNOWLEDGMENTS

This work was supported in part by the National Science Foundation under grant 1903649 (MK). Further support from the University of Miami and Ball State University (E.M.Z.) is acknowledged. The authors thank Professor Dennis A. Hansell and Lillan Custals for assistance with the TOC analysis. S.D. thanks Sylvester Comprehensive Cancer Center for financial support.

■ REFERENCES

(1) Hu, A.; Zhang, X.; Luong, D.; Oakes, K. D.; Servos, M. R.; Liang, R.; Kurdi, S.; Peng, P.; Zhou, Y. Adsorption and photocatalytic degradation kinetics of pharmaceuticals by TiO_2 nanowires during water treatment. *Waste Biomass Valorization* **2012**, *3*, 443−449.

(2) Chala, S.; Wetchakun, K.; Phanichphant, S.; Inceesungvorn, B.; Wetchakun, N. Enhanced visible-light-response photocatalytic degradation of methylene blue on Fe-loaded $BiVO_4$ photocatalyst. *J. Alloys Compd.* **2014**, *597*, 129−135.

(3) Ge, L.; Liu, J. Efficient visible light-induced photocatalytic degradation of methyl orange by QDs sensitized CdS-Bi_2WO_6. *Appl. Catal., B* **2011**, *105*, 289−297.

(4) Gao, Q.; Wu, X.; Fan, Y.; Zhou, X. Low temperature fabrication of nanoflower arrays of rutile TiO_2 on mica particles with enhanced photocatalytic activity. *J. Alloys Compd.* **2013**, *579*, 322−329.

(5) Hsiao, Y.-C.; Wu, T.-F.; Wang, Y.-S.; Hu, C.-C.; Huang, C. Evaluating the sensitizing effect on the photocatalytic decoloration of dyes using anatase-TiO_2. *Appl. Catal., B* **2014**, *148−149*, 250−257.

(6) Li, S.; Zhao, Z.; Huang, Y.; Di, J.; Jia, Y.; Zheng, H. Hierarchically structured WO_3−CNT@TiO_2NS composites with enhanced photocatalytic activity. *J. Mater. Chem. A* **2015**, *3*, 5467−5473.

(7) Chatterjee, D.; Dasgupta, S. Visible light induced photocatalytic degradation of organic pollutants. *J. Photochem. Photobiol., C* **2005**, *6*, 186−205.

(8) Li, G.; Zhang, D.; Yu, J. C. Ordered mesoporous $BiVO_4$ through nanocasting: A superior visible light-driven photocatalyst. *Chem. Mater.* **2008**, *20*, 3983−3992.

(9) Martínez-de la Cruz, A.; García-Pérez, U. M.; Sepúlveda-Guzmán, S. Characterization of the visible-light-driven $BiVO_4$ photocatalyst synthesized via a polymer-assisted hydrothermal method. *Res. Chem. Intermed.* **2013**, *39*, 881−894.

(10) Tokunaga, S.; Kato, H.; Kudo, A. Selective preparation of monoclinic and tetragonal $BiVO_4$ with scheelite structure and their photocatalytic properties. *Chem. Mater.* **2001**, *13*, 4624−4628.

(11) Bierlein, J. D.; Sleight, A. W. Ferroelasticity in $BiVO_4$. *Solid State Commun.* **1975**, *16*, 69−70.

(12) Fan, H.; Jiang, T.; Li, H.; Wang, D.; Wang, L.; Zhai, J.; He, D.; Wang, P.; Xie, T. Effect of $BiVO_4$ crystalline phases on the photoinduced carriers behavior and photocatalytic activity. *J. Phys. Chem. C* **2012**, *116*, 2425−2430.

(13) Kudo, A.; Omori, K.; Kato, H. A novel aqueous process for preparation of crystal form-controlled and highly crystalline $BiVO_4$ powder from layered vanadates at room temperature and its photocatalytic and photophysical properties. *J. Am. Chem. Soc.* **1999**, *121*, 11459−11467.

(14) Park, Y.; McDonald, K. J.; Choi, K.-S. Progress in bismuth vanadate photoanodes for use in solar water oxidation. *Chem. Soc. Rev.* **2013**, *42*, 2321−2337.

(15) Long, M.; Cai, W.; Cai, J.; Zhou, B.; Chai, X.; Wu, Y. Efficient Photocatalytic Degradation of Phenol over $Co_3O_4/BiVO_4$ Composite under Visible Light Irradiation. *J. Phys. Chem. B* **2006**, *110*, 20211−20216.

(16) Wang, M.; Che, Y.; Niu, C.; Dang, M.; Dong, D. Effective visible light-active boron and europium co-doped $BiVO_4$ synthesized by sol−gel method for photodegradion of methyl orange. *J. Hazard. Mater.* **2013**, *262*, 447−455.

(17) Guo, M.; Wang, Y.; He, Q.; Wang, W.; Wang, W.; Fu, Z.; Wang, H. Enhanced photocatalytic activity of S-doped BiVO4 photocatalysts. *RSC Adv.* **2015**, *5*, 58633−58639.

(18) Xu, X.; Du, M.; Chen, T.; Xiong, S.; Wu, T.; Zhao, D.; Fan, Z. New insights into Ag-doped $BiVO_4$ microspheres as visible light photocatalysts. *RSC Adv.* **2016**, *6*, 98788−98796.

(19) Kohtani, S.; Tomohiro, M.; Tokumura, K.; Nakagaki, R. Photooxidation reactions of polycyclic aromatic hydrocarbons over pure and Ag-loaded $BiVO_4$ photocatalysts. *Appl. Catal., B* **2005**, *58*, 265−272.

(20) Li, H.-b.; Zhang, J.; Huang, G.-y.; Fu, S.-h.; Ma, C.; Wang, B.-y.; Huang, Q.-r.; Liao, H.-w. Hydrothermal synthesis and enhanced photocatalytic activity of hierarchical flower-like Fe-doped $BiVO_4$. *Trans. Nonferrous Met. Soc. China* **2017**, *27*, 868−875.

(21) Regmi, C.; Kshetri, Y. K.; Kim, T.-H.; Pandey, R. P.; Lee, S. W. Visible-light-induced Fe-doped $BiVO_4$ photocatalyst for contaminated water treatment. *Mol. Catal.* **2017**, *432*, 220−231.

(22) Liu, S.; Li, X.; Meng, X.; Chen, T.; Kong, W.; Li, Y.; Zhao, Y.; Wang, D.; Zhu, S.; Cheema, W. A.; Pan, J. Enhanced visible/near-infrared light harvesting and superior charge separation via 0D/2D all-carbon hybrid architecture for photocatalytic oxygen evolution. *Carbon* **2020**, *167*, 724−735.

(23) Liu, S.; Pan, J.; Li, X.; Meng, X.; Yuan, H.; Li, Y.; Zhao, Y.; Wang, D.; Ma, J.; Zhu, S.; Kong, L. In situ modification of $BiVO_4$ nanosheets on graphene for boosting photocatalytic water oxidation. *Nanoscale* **2020**, *12*, 14853−14862.

(24) Zhang, L.; Tan, G.; Wei, S.; Ren, H.; Xia, A.; Luo, Y. Microwave hydrothermal synthesis and photocatalytic properties of $TiO_2/BiVO_4$ composite photocatalysts. *Ceram. Int.* **2013**, *39*, 8597−8604.

(25) Yan, M.; Wu, Y.; Yan, Y.; Yan, X.; Zhu, F.; Hua, Y.; Shi, W. Synthesis and characterization of novel $BiVO_4/Ag_3VO_4$ heterojunction with enhanced visible-light-driven photocatalytic degradation of dyes. *ACS Sustainable Chem. Eng.* **2016**, *4*, 757−766.

(26) Shenawi-Khalil, S.; Uvarov, V.; Fronton, S.; Popov, I.; Sasson, Y. A novel heterojunction BiOBr/Bismuth Oxyhydrate photocatalyst with highly enhanced visible light photocatalytic properties. *J. Phys. Chem. C* **2012**, *116*, 11004−11012.

(27) Zalfani, M.; van der Schueren, B.; Hu, Z.-Y.; Rooke, J. C.; Bourguiga, R.; Wu, M.; Li, Y.; Van Tendeloo, G.; Su, B.-L. Novel 3DOM $BiVO_4/TiO_2$ nanocomposites for highly enhanced photocatalytic activity. *J. Mater. Chem. A* **2015**, 3, 21244−21256.

(28) Su, Q.; Li, Y.; Hu, R.; Song, F.; Liu, S.; Guo, C.; Zhu, S.; Liu, W.; Pan, J. Heterojunction photocatalysts based on 2D materials: the role of configuration. *Adv. Sustainable Syst.* **2020**, *4*, 2000130.

(29) He, T.; Wu, D.; Tan, Y. Fabrication of BiOI/$BiVO_4$ heterojunction with efficient visible-light-induced photocatalytic activity. *Mater. Lett.* **2016**, *165*, 227−230.

(30) Ye, K.-H.; Chai, Z.; Gu, J.; Yu, X.; Zhao, C.; Zhang, Y.; Mai, W. BiOI−$BiVO_4$ photoanodes with significantly improved solar water splitting capability: p−n junction to expand solar adsorption range and facilitate charge carrier dynamics. *Nano Energy* **2015**, *18*, 222−231.

(31) Huang, H.; He, Y.; Du, X.; Chu, P. K.; Zhang, Y. A general and facile approach to heterostructured core/shell $BiVO_4$/BiOI p−n junction: room-temperature in situ assembly and highly boosted visible-light photocatalysis. *ACS Sustainable Chem. Eng.* **2015**, *3*, 3262−3273.

(32) Ye, Z.; Xiao, X.; Chen, J.; Wang, Y. Fabrication of $BiVO_4$/BiOBr composite with enhanced photocatalytic activity by a CTAB-assisted polyol method. *J. Photochem. Photobiol., A* **2019**, *368*, 153−161.

(33) Feng, C.; Wang, D.; Jin, B.; Jiao, Z. The enhanced photocatalytic properties of BiOCl/$BiVO_4$ p−n heterojunctions via plasmon resonance of metal Bi. *RSC Adv.* **2015**, *5*, 75947−75952.

(34) Zhao, L.; Zhang, X.; Fan, C.; Liang, Z.; Han, P. First-principles study on the structural, electronic and optical properties of BiOX (X=Cl, Br, I) crystals. *Phys. B* **2012**, *407*, 3364−3370.

(35) Zhang, X.; Ai, Z.; Jia, F.; Zhang, L. Generalized One-Pot Synthesis, Characterization, and Photocatalytic Activity of Hierarchical BiOX (X = Cl, Br, I) Nanoplate Microspheres. *J. Phys. Chem. C* **2008**, *112*, 747−753.

(36) He, Z.; Shi, Y.; Gao, C.; Wen, L.; Chen, J.; Song, S. BiOCl/$BiVO_4$ p−n heterojunction with enhanced photocatalytic activity under visible-light irradiation. *J. Phys. Chem. C* **2014**, *118*, 389−398.

(37) Cao, J.; Zhou, C.; Lin, H.; Xu, B.; Chen, S. Surface modification of *m*-$BiVO_4$ with wide band-gap semiconductor BiOCl to largely improve the visible light induced photocatalytic activity. *Appl. Surf. Sci.* **2013**, *284*, 263−269.

(38) Xiang, Z.; Wang, Y.; Zhang, D.; Ju, P. BiOI/$BiVO_4$ p-n heterojunction with enhanced photocatalytic activity under visible-light irradiation. *J. Ind. Eng. Chem.* **2016**, *40*, 83−92.

(39) Zhang, Y.; Li, W.; Sun, Z.; Zhang, Q.; Wang, L.; Chen, Z. In-situ synthesis of heterostructured $BiVO_4$/BiOBr core-shell hierarchical mesoporous spindles with highly enhanced visible-light photocatalytic performance. *J. Alloys Compd.* **2017**, *713*, 78−86.

(40) Regmi, C.; Dhakal, D.; Kim, T.-H.; Yamaguchi, T.; Lee, S. W. Fabrication of Ag-decorated BiOBr-m$BiVO_4$ dual heterojunction composite with enhanced visible light photocatalytic performance for degradation of malachite green. *Nanotechnology* **2018**, *29*, 154001.

(41) Pálmai, M.; Zahran, E. M.; Angaramo, S.; Bálint, S.; Pászti, Z.; Knecht, M. R.; Bachas, L. G. Pd-decorated *m*-$BiVO_4$/BiOBr ternary composite with dual heterojunction for enhanced photocatalytic activity. *J. Mater. Chem. A* **2017**, *5*, 529−534.

(42) Das, G. C.; Das, B.; Sarma, N. S.; Medhi, O. K. Synthesis, structure and properties of cetyltrimethylammonium polyiodides. *Polyhedron* **2012**, *37*, 14−20.

(43) Lin, H.; Ye, H.; Li, X.; Cao, J.; Chen, S. Facile anion-exchange synthesis of BiOI/BiOBr composite with enhanced photoelectrochemical and photocatalytic properties. *Ceram. Int.* **2014**, *40*, 9743−9750.

(44) Ganose, A. M.; Cuff, M.; Butler, K. T.; Walsh, A.; Scanlon, D. O. Interplay of orbital and relativistic effects in Bismuth Oxyhalides: BiOF, BiOCl, BiOBr, and BiOI. *Chem. Mater.* **2016**, *28*, 1980−1984.

(45) Huang, J.; He, S.; Goodsell, J. L.; Mulcahy, J. R.; Guo, W.; Angerhofer, A.; Wei, W. D. Manipulating atomic structures at the Au/TiO_2 interface for O_2 activation. *J. Am. Chem. Soc.* **2020**, *142*, 6456−6460.

(46) Li, L.; Salvador, P. A.; Rohrer, G. S. Photocatalysts with internal electric fields. *Nanoscale* **2014**, *6*, 24−42.

(47) Lv, D.; Zhang, D.; Pu, X.; Kong, D.; Lu, Z.; Shao, X.; Ma, H.; Dou, J. One-pot combustion synthesis of $BiVO_4$/BiOCl composites with enhanced visible-light photocatalytic properties. *Sep. Purif. Technol.* **2017**, *174*, 97−103.